Electrically-Small, Low-Profile, Huygens Circularly Polarized Antenna

Wei Lin, *Member, IEEE* and Richard W. Ziolkowski, *Fellow, IEEE*

***Abstract*—The design, simulation studies, and experimental verification of an electrically-small, low-profile, broadside-radiating Huygens circularly-polarized (HCP) antenna are reported. To realize its unique CP cardioid-shaped radiation characteristics in a compact structure, two pairs of the metamaterial-inspired near-field resonant parasitic (NFRP) elements, the Egyptian axe dipole (EAD) and the capacitively loaded loop (CLL), are integrated into a crossed-dipole configuration. The EAD (CLL) elements act as the orthogonal electric dipole (magnetic dipole) radiators. Balanced broadside-radiated electric and magnetic field amplitudes with the requisite 90° phase difference between them are realized by exciting these two pairs of electric and magnetic dipoles with a specially designed, unbalanced crossed-dipole structure. The electrically small (*ka* = 0.73) design operates at 1575 MHz. It is low profile, 0.04λ_0, and its entire volume is only 0.0018 λ_0^3. A prototype of this optimized HCP antenna system was fabricated, assembled, and tested. The measured results are in good agreement with their simulated values. They demonstrate that the prototype HCP antenna resonates at 1584 MHz with a 0.6 dB axial ratio, and produces the predicted Huygens cardioid-shaped radiation patterns. The measured HCP peak realized LHCP gain was 2.7 dBic and the associated front-to-back ratio was 17.7 dB.**

***Index Terms*—Circular polarization (CP), electrically small antennas, global positioning system (GPS), Huygens source, near-field resonant parasitic (NFRP) elements**

I. Introduction

Electrically-small antennas (ESAs) have received much attention recently with the rapid development of modern wireless systems and their requirements for ever more compact, mobile devices and terminals. Notable applications include communication systems [1]-[3]; biomedical systems [4]; and RFIDs [5], [6]. Moreover, because of their associated narrow bandwidths, they are very appropriate for many compact electronic device applications, for example, for global positioning (GPS) [7] and wireless power transfer (WPT) systems [8], [9].

Manuscript received on Jun. 04, 2017, revised Sep. 04, 2017, revised Oct. 26, 2017, revised Dec. 08, 2017

This work was supported in part by the Australian Research Council grant number DP160102219.

Wei Lin is with the University of Technology Sydney, Global Big Data Technologies Centre, Ultimo NSW 2007, Australia (E-mail: wei.lin@uts.edu.au).

Richard. W. Ziolkowski is with the University of Technology Sydney, Global Big Data Technologies Centre, Ultimo NSW 2007, Australia, and the Department of Electrical and Computer Engineering, University of Arizona, Tucson, AZ 85721, USA (E-mail: Richard.Ziolkowski@uts.edu.au).

The antenna characteristics for these types of applications have some unique specifications. First, these ESAs should have sufficiently broad directivity and decent radiation efficiency. Second, it is preferred that they radiate circular polarization to combat multipath and to eliminate polarization mismatch [10], [11]. Broadside-radiated, CP cardioid patterns would help facilitate meeting all of these criteria.

On the other hand, it is very challenging for ESAs to achieve all of these desired radiation characteristics. Both conventional and more recent ESA designs [12] – [18] commonly exhibit either electric or magnetic dipole-like radiation performance and are constrained by basic physics [19] – [21]. Consequently, their peak realized gain and front-to-back ratio (FTBR) values are generally quite low. While the simultaneous excitation of electric and magnetic dipole-like performance has been considered with different three-dimensional sphere-based antennas [22] – [24], practical planar Huygens source versions have not been reported at the RF frequencies of interest herein.

To achieve the desired directional and CP performance characteristics without increasing the effective area of the antenna, metamaterial-inspired near-field resonant parasitic (NFRP) Huygens (complementary) dipole antennas have been realized [25] – [27]. In comparison with other complementary source antennas [28] – [33], they are electrically-small; and their profile and volume are significantly less. Unfortunately, these Huygens ESAs are all linearly-polarized and, hence, not suitable for the noted applications. Although the concept of a 28 GHz CP Huygens antenna has been studied [34], an HCP ESA was not attained in practice.

In this paper, we report the first successful design and realization of a low profile (~0.04 λ_0), broadside-radiating, electrically-small (*ka* = 0.73) Huygens circular polarization (HCP) antenna operating at 1575 MHz. The prototype is compact; its overall volume is only $\pi\ (22.5)^2 \times 7.79\ \text{mm}^3 = 0.0018\ \lambda_0^3$. This is a more than 88 times and 92 times smaller volume than the previously reported HCP antennas in [35] and [36], respectively. Measurements of the prototype demonstrate a Huygens CP radiation pattern at 1584 MHz (only 0.57% different from the design value) with a peak realized LHCP gain of 2.7 dBic, a broadside axial ratio (AR) value of 0.6 dB, a 3-dB AR beamwdith larger than 180°, and a front-to-back ratio (FTBR) equal to 17.7 dB. The HCP design concept is discussed in Sec. II. The actual antenna structure is described in Sec. III. It consists of two pairs of the Egyptian axe dipole (EAD) and the capacitively loaded loop (CLL) near-field resonant parasitic

(NFRP) elements excited by an unbalanced crossed-dipole structure. This feed structure is driven with a single, standard 50-Ω coaxial feedline. The engineering design knowledge gleaned from simulation studies of the key parameters, which led to an optimized design, is reviewed in Sec. IV. An HCP prototype based on this design was realized. The fabricated antenna components, assembly, and experimental results are described in Sec. V. Finally, conclusions are given in Sec. VI.

All simulation results reported in this paper were obtained with the ANSYS high frequency structure simulator (HFSS) version 17. The materials associated with these simulation models incorporated all of their known properties. The HCP antenna prototype was fabricated with 0.5 oz (17 μm thick) Rogers™ 5880 copper-cladded substrate, which has a relative permittivity and permeability equal to 2.2 and 1.0, respectively, and a loss tangent of 0.0009.

II. HCP Design Concepts

The basic Huygens CP antenna design concept is straightforward. It is well known that a Huygens LP dipole antenna can be achieved by combining an electric dipole with an orthogonally oriented magnetic dipole in such a manner that they coherently produce in-phase equal-amplitude far fields as thoroughly discussed in [28]–[29]. To achieve the electrically-small design, i.e., to have $ka < 1$, where a is the radius of the smallest sphere enclosing the entire antenna structure and k is the free-space wavenumber at the operational frequency [37]–[39], the metamaterial-inspired NFRP elements used to achieve the HLP systems [25]–[27] were adopted. They are depicted in Fig. 1(a). The Egyptian axe dipole (EAD) element excited with the driven dipole antenna acts as the electric dipole radiator. Similarly, the capacitively loaded loop (CLL) element also excited with the driven dipole element acts as the magnetic dipole radiator. Arranging two orthogonal electrically small HLP antennas with a 90° phase difference between them, as illustrated in Fig. 1(b), one obtains the desired CP cardioid-shaped 3D radiation pattern. It consists of two pairs of the orthogonal electric and magnetic dipoles. The dipoles I_{e1} and I_{m1} (I_{e2} and I_{m2}) are orthogonally oriented in-phase. The two electric, I_{e1} and I_{e2} (magnetic, I_{m1} and I_{m2}) dipoles are also orthogonally oriented, but are excited with a 90° phase difference.

III. HCP Antenna Optimized Design

To realize the two pairs of orthogonally-oriented electric and magnetic dipoles depicted in Fig. 1(b), we have systematically integrated two EADs and two CLLs into the radiating entity shown in Fig. 2. The HCP antenna system consists of three disc-shaped substrates, four metallic layers, and four vertical connecting copper rods. The crossed EAD and CLL elements in this structure are readily visualized by correlating Figs. 2(a) to 2(d). Standard printed circuit board (PCB) manufacturing technology is applied for fabricating all of these components, and their assembly is straightforward.

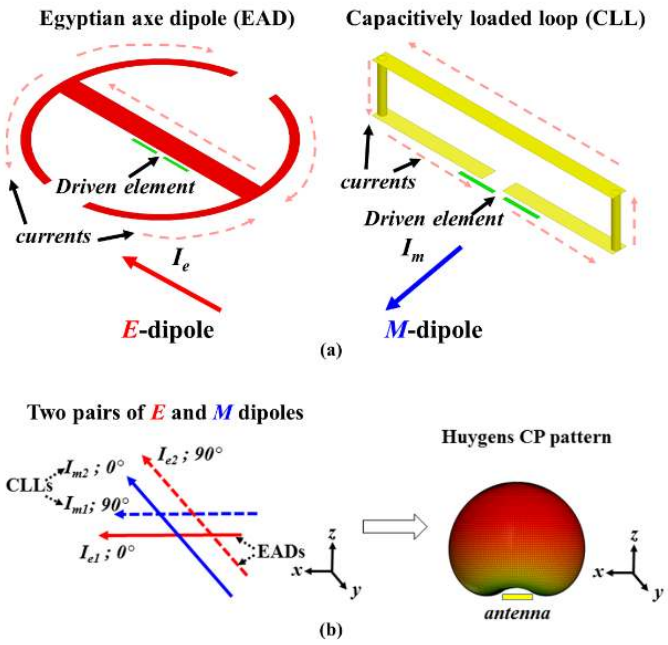

Fig. 1. HCP NFRP antenna design concepts. (a) Electric and magnetic dipole responses achieved, respectively, by exciting the electrically-small Egyptian axe dipole (EAD) and the capacitively loaded loop (CLL) NFRP elements with a driven electric dipole antenna. (b) Two pairs of orthogonal, balanced, electric (EAD) and magnetic (CLL) dipole elements produce a CP cardioid 3D directivity pattern.

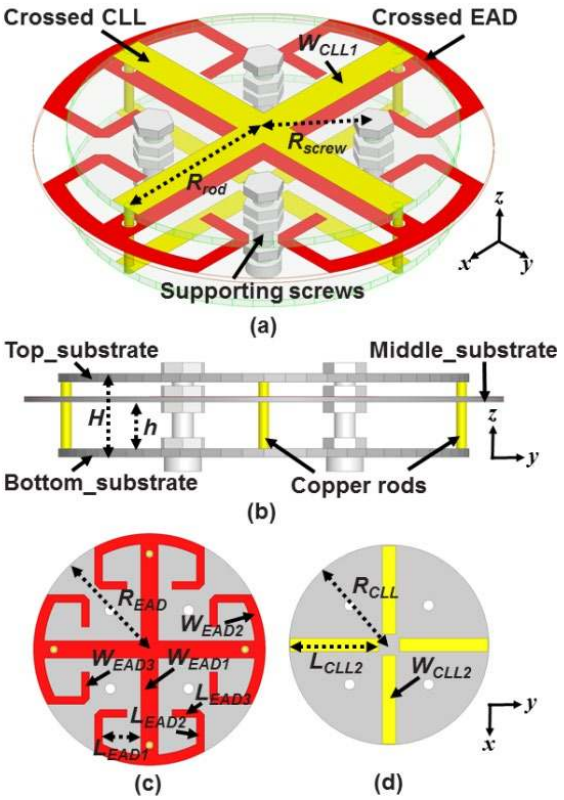

Fig. 2. HCP antenna configuration and design parameters. (a) Perspective view. (b) Side view of the whole structure. (c) Top view of the middle disc. (d) Top view of the bottom disc.

Each of the three layers is a disc-shaped piece of the

Rogers™ 5880 copper-cladded substrate. The top and bottom discs are 0.7874 mm thick and have the same radius R_{CLL}; the middle layer is 0.508 mm thick and has a slightly larger radius R_{EAD}. The upper-most metallization layer is the top surface of the top disc. The top of the crossed CLL element structure is etched in it. The bottom metallic layer of this disc is etched away. The bottom layer of the crossed CLL structure, shown in Fig. 2(d), is etched on the top surface of the bottom-most disc. The four vertical copper cods connect these upper and bottom pieces, as shown in Figs. 2(a) and 2(b), to form the complete crossed CLL structure. The crossed EAD radiator, shown in Fig. 2(c) is etched on the top surface of the middle disc. The terminating heads of the EAD arms are designed to achieve a compact structure, while avoiding overlaps with any other component. The four copper rods of the CLL structure pass through holes in the middle layer and through the EAD metallization without touching it. The last metallization layer, on the bottom surface of the bottom disc, is the excitation structure, i.e., the directly driven elements. It will be described in detail in the following section. Four plastic screws are used to give mechanical stability to the whole structure and to maintain the separation distances between each layer. The antenna configuration is very compact, lightweight, and cost-effective. It was designed to operate at the GPS L1 frequency, 1.575 GHz. It is electrically small with ka = 0.73 and low profile with its overall height being only 0.04 λ_0. The overall volume of the antenna is only π $(22.5)^2 \times 7.79$ mm^3 = 0.0018 λ_0^3. The values of the structural parameters of the optimized HCP antenna are given in Table I.

TABLE I:
HCP ANTENNA DESIGN PARAMETERS (DIMENSIONS IN MILLIMETERS)

Parameter	Description	Value
R_{rod}	Radius of the copper rod from center	18.5
R_{screw}	Radius of the plastic screws from center	10.6
W_{CLL1}	Width of the upper CLLs	3.5
H	Overall height of the HCP antenna	7.79
h	Distance of the EAD to bottom substrate	4.36
R_{EAD}	Radius of the EAD substrate	22.5
W_{EAD1}	Width of center straight part of the EAD	3.3
W_{EAD2}	Width of arched part of the EAD	2.0
W_{EAD3}	Width of bended part of the EAD	1.5
L_{EAD1}	Length of arched part of the EAD	7.35
L_{EAD2}	Length of 1st bended part of the EAD	5.42
L_{EAD3}	Length of 2nd bended part of the EAD	4.7
R_{CLL}	Radius of the CLL substrates	19.5
L_{CLL}	Length of the bottom strips of CLL	17
W_{CLL2}	Width of the bottom strips of CLL	2.5

A. Excitation technique

Three distinct excitation techniques, each having unique input impedance characteristics, were developed for the current and future HCP antennas. They include spiral, delayed loop, and unbalanced cross-dipole feeding structures. The set provides a range of input impedance responses for these ESAs that enables matching them to inductive, capacitive or 50-Ω loads while still producing effective HCP responses. The unbalanced crossed-dipole version proved to be an effective excitation mechanism appropriate to realize our optimized 50-Ω design.

This unbalanced cross-dipole excitation structure is shown in Fig. 3. Its arms have lengths L_{d1} and L_{d2} which are directly fed by a 50-Ω ohm coaxial cable as illustrated (one pair connected to the center conductor, the other pair connected to the outer conductor). Being tuned to a 1.575 GHz (190.34 mm) source, the total length ($2 \times L_{d2}$) of the horizontal dipole (along the y-axis) is 12.1 mm and the total length ($2 \times L_{d1}$) of the vertical dipole (along the x-axis) is 11.3 mm. The 0.8 mm offset between the two orthogonal dipoles provides the requisite 90° phase difference at this resonance frequency. This design concept was inspired by the quadrifilar helical antennas reported in [40] and [41]. The CP behavior in those designs is realized by offsetting the resonances of the two helical radiators, one to be a little higher and one to be a little lower than the desired operating frequency. This is essentially the same approach used for the dual-band CP GPS antenna reported in [42]. It was further determined that the polarization type is regulated by the excitation structure. If L_{d2} is longer than L_{d1}, as in the prototype design, LHCP radiation is observed. On the other hand, RHCP radiation is realized simply by swapping the lengths of these two arms.

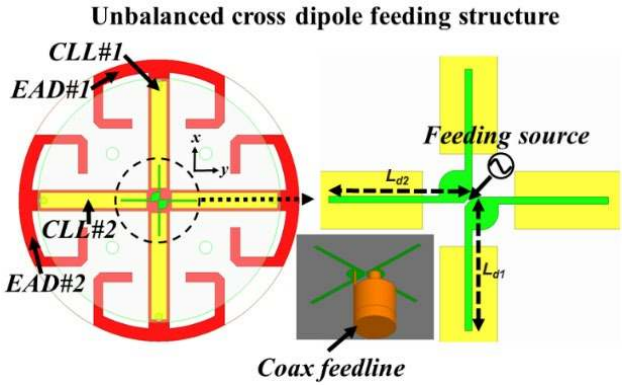

Fig. 3. Unbalanced crossed-dipole excitation structure for the HCP ESA. (a) Bottom view of the antenna. (b) Enlarged view of the driven crossed-dipole element, the insert showing how the coax feedline is attached directly to the arms of its dipoles.

B. Operating Characteristics of the Final Design

Fig. 4(a) presents the simulated input impedance of the HCP antenna with the unbalanced crossed-dipole excitation structure as a function of the source frequency. Two resonances appear around the targeted GPS L1 operational frequency, 1.575 GHz, with the real part being very close to 50-Ω. The corresponding Smith chart plot shown in Fig. 4(b) clearly shows this dual-resonance behavior, having a dip in the impedance circle. The frequency corresponding to this dip is exactly where the best CP radiation (lowest AR value) is generated. Fig. 5(a) provides the simulated $|S_{11}|$ and AR values as functions of the source frequency. Very good impedance matching to the 50-Ω source was obtained and the frequency of the lowest AR value falls inside the 13MHz, -10-dB impedance bandwidth, from 1569-1582 MHz. The minimum $|S_{11}|$ value is – 29.2 dB at 1572 MHz, while the lowest AR value is 0.74 dB at 1576 MHz. The

simulated HCP gain patterns are shown in Fig. 5(b). Excellent behavior is demonstrated. These two-dimensional patterns for the φ = 0° and φ = 90° planes at 1.575 GHz are identical with peak realized gains of 3.3 dBic; wide 3-dB power beamwidths, from ±69°; and very large FTBR values, 21 dB. The radiation efficiency, 76%, is quite decent for such a complex, compact structure.

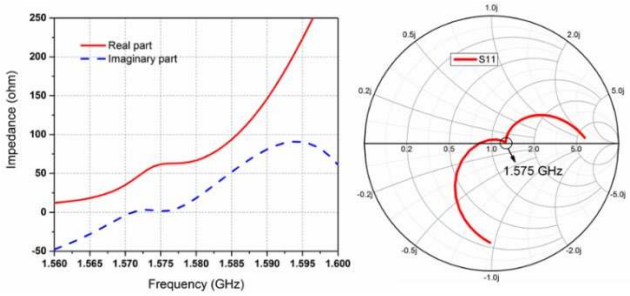

(a) (b)

Fig. 4. Simulated results of the HCP ESA with the unbalanced crossed-dipole excitation structure. (a) Input impedance values. (b) $|S_{11}|$ values plotted on a Smith chart as functions of the source frequency.

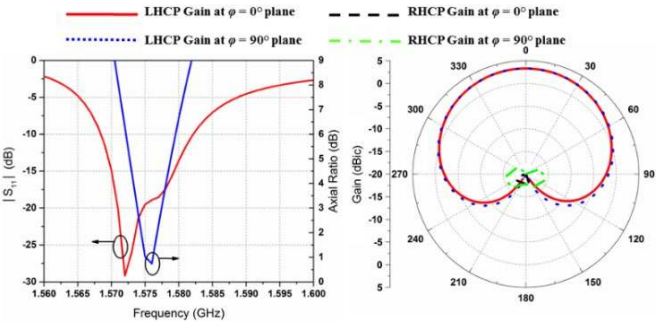

(a) (b)

Fig. 5. Simulated results of the HCP ESA with the unbalanced crossed-dipole excitation structure. (a) $|S_{11}|$ and AR values as functions of the source frequency. (b) The LCHP and RCHP realized gain patterns at 1.575 GHz.

The operating mechanisms associated with the HCP performance are explained with the current distributions on the crossed EAD and CLL elements and on the excitation structure. These are shown in Fig. 6. At t = 0, Fig. 6(a) shows that the currents are concentrated on EAD#1 and on CLL#2 and EAD#2. The currents on EAD#1 form the electric dipole I_{e1}. The total combined currents on CLL#2 and EAD#2 form the loop current that generates the magnetic dipole I_{m2}. On the other hand, when t = 3T/4, Fig. 6(d) shows that the currents are predominant on EAD#2 and on CLL#1 and EAD#1. The electric dipole current moment I_{e2} is generated by the currents on EAD#2. The corresponding magnetic dipole current I_{m1} is generated from the loop current resulting from the combination of the currents on CLL#1 and EAD#1. It is noted, however, that the magnetic dipole moments have a 90° phase difference with respect to their electric counterparts. The magnetic dipole moment I_{m1} is in phase with the electric dipole moment I_{e1} at t = 0, while I_{m2} is in phase with I_{e2} at t = T/4. These orientations of the electric and magnetic dipoles are shown; they generate the broadside Huygens pattern. Moreover it is noted that the phase differences of both of these electric and magnetic dipole pairs are rotated by 90° clockwise over this quarter period which generates the CP radiation. Figs. 6(b) and 6(c) further illustrate that this clockwise rotation continues over these two quarter periods. The pair I_{e1} and I_{m1} are in phase again at t = 2T/4; the pair pair I_{e2} and I_{m2} are in phase again at t = 3T/4. Again, these two pairs are out of phase with each other by T/4, i.e., by 90° clockwise. Since the clockwise rotation is observed looking opposite from the direction of propagation of the outgoing wave, the dominant state is LHCP in agreement with the results shown in Fig. 5 (b).

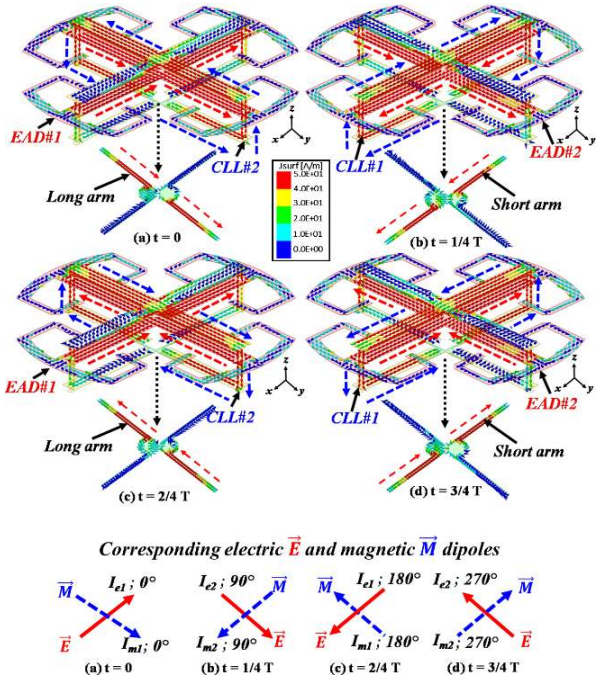

Fig. 6. Current distributions on the crossed EAD and CLL elements and the crossed-dipole excitation structure at 1.575 GHz at four different quarter-periods. The clockwise rotation of the resonant currents confirms the LHCP behavior of the antenna shown in Fig. 5(b).

IV. Design Studies and Guidelines

Two key parameters in the designs of the crossed EAD and CLL structures were identified and studied. They impact achieving the targeted operating frequency and the mode that realizes the cancelling backfire HCP radiation. Design guidelines were established from these parameter studies.

(a) Crossed EAD and CLL element dimensions

The sizes of the resonating EAD and CLL elements determine the coarse operating frequency of the HCP antenna system. Fig. 7 presents the simulated $|S_{11}|$ and AR values as functions of the source frequency when the radius of the EAD, R_{EAD}, and the radius of the CLL, R_{CLL}, discs are, respectively, 22.3 and 18.3 mm; 22.4 and 18.4 mm; and 22.5 and 18.5 mm. It is observed immediately that the operating frequency is very dependent on these dimensions due to the highly resonant nature of the HCP structure. In the final design, the choices: R_{EAD} = 22.5 mm and R_{CLL}= 18.5 mm, were made to attain the targeted GPS L1 frequency of 1.575 GHz.

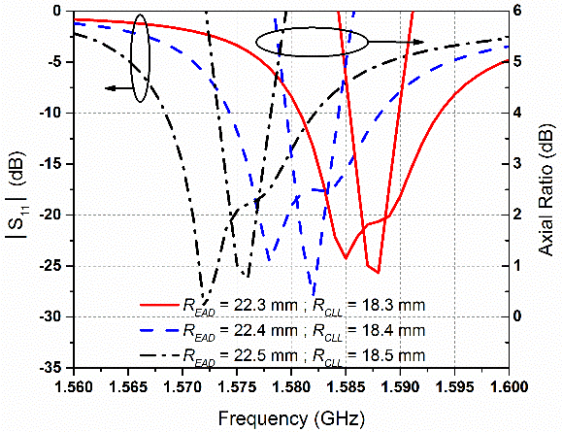

Fig. 7. Simulated $|S_{11}|$ and AR values of the HCP ESA with the unbalanced crossed-dipole excitation structure as functions of the source frequency when the radii of the EAD, R_{EAD}, and the CLL, R_{CLL}, discs are varied.

While the broadside Huygens radiation mode has been demonstrated with the fields propagating into the +z half-space, the antenna structure can produce a backfire Huygens radiation mode simply by adjusting the coupling between the crossed EAD and CLL elements. This coupling determines the phase between the currents on them. In agreement with the initial Huygens LP ESA design concept [25], by increasing the height of the EAD 0.3 mm from the optimized design and retuning the design parameters slightly to bring it back into resonance, the currents on this electric dipole witness a 180° phase difference. In essence, the relative distance between the phase centers of the electric and magnetic dipoles have been changed and the backfire mode is produced. Simply changing the parameters: h = 4.66 mm and RCLL= 19.0 mm, a LHCP backfire Huygens mode is attained with performance characteristics nearly identical to the broadside version.

(b) Realized design guidelines

From the reported parameter studies and many other analyses and simulations, a general design guideline was developed to realize such an HCP antenna for any specified frequency of operation.

The first step is to design the CLL element to resonate at a frequency a bit higher than the targeted operating frequency. This is necessary because the resonance frequency will be pulled lower when the capacitive EAD element is integrated with it. The total length of the CLL should be about 0.45 λ_0. It is noted that in this initial design phase, the driven elements can simply be short dipoles with the same arm lengths instead of the more complicated unbalanced crossed-dipole excitation structure.

The second step is to integrate the EAD element into the structure below the top surface of CLL element. The length of the straight section of the EAD is around 0.2 λ_0. The detailed shape of the arc-heads of the straight section is modified to tune the resonance frequency to overlap with that of the CLL element. The gap distance between the top of the EAD element and the top of the CLL element should be about 0.007 λ_0.

The third step is to carefully adjust the dimensions and the gap between the EAD and CLL elements to fine tune the whole system to be resonating at the targeted operating frequency and to be generating the desired direction for the Huygens radiation mode (broadside or backfire).

The last step is to replace the short symmetric driven dipoles with the unbalanced crossed-dipole excitation structure. The unbalanced length should be about 6% longer than the shorter of the driven dipoles. When the recognized dip in the $|S_{11}|$ values plotted as a function of the source frequency on the Smith chart is observed, the HCP radiation has been realized. The operating frequency of the best CP radiation is located at that dip. The dimensions of the pieces of the EAD and CLL elements can be adjusted slightly if finer tuning of the operating frequency is needed.

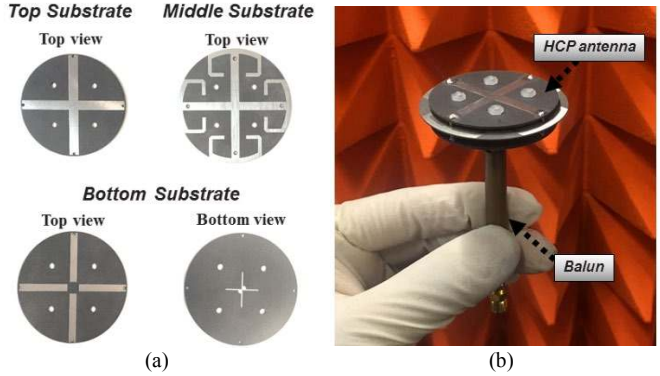

Fig. 8. HCP ESA. (a) Photos of the fabricated components. (b) The assembled prototype with a sleeve balun.

V. Measured Results

The components of a prototype of the HCP antenna were fabricated and assembled as shown in Figs. 8(a) and 8(b), respectively. The three disc-shaped substrate structures were fabricated with standard PCB manufacturing technologies. The four copper rods with their 1.0 mm diameter were soldered to the upper and bottom strips to complete the crossed CLL structure. As designed, the entire prototype was electrically-small (ka = 0.73), low profile (~ 0.04λ_0) and very lightweight. To obtain more accurate radiation characteristics, a long, 60 mm, 50-Ω coaxial cable feedline was used in the measurement set-up. However, because of this cable length, the copper sleeve balun shown in Fig. 8(b) was added to prevent the excitation of any leakage currents on the outer surface of the coax line. The length of the balun was 46.0 mm; its diameter was 7.0 mm. The thickness of the copper used to fabricate it was 0.5 mm.

The $|S_{11}|$ values of the prototype were measured with a Keysight Vector Network Analyzer; the radiation patterns were measured with a SATIMO (MVG StarLab) near-field system [43]. The latter was selected because of it known successful performance when measuring patterns and their FTBR values [30, 31]. The measured and simulated $|S_{11}|$ and AR values are plotted in Fig. 9(a) and the measured $|S_{11}|$ values are Smith chart plotted in Fig. 9(b) as functions of the source frequency. The measured and simulated results agree reasonably well. The 3-dB AR bandwidth is 4.0 MHz from 1582.5 to 1586.5 MHz.

The AR values at 1583, 1584, 1585 and 1586 MHz are 1.9, 0.6, 0.8 and 2.0, respectively. The measured AR bandwidth agrees very well with its simulated value. Due to fabrication and assembly tolerances, the measured operating frequency shifted slightly higher, 9 MHz (0.57%), to 1584 MHz. As demonstrated in our parameter studies, this discrepancy is quite reasonable since slight changes (0.1 mm) in either the radius of the EAD or CLL elements will cause a similar frequency shift. Moreover, additional simulations have demonstrated that the presence of the balun introduces a slight frequency shift towards a higher band. In particular, the operating frequency moves only 3 MHz to 1578 MHz from the original 1575 MHz when the antenna is fed with the 60 mm long coax feedline and the balun is present. This coincides with the fact that the current distributions on the balun are significantly less than those on the EAD and CLL NFRP elements.

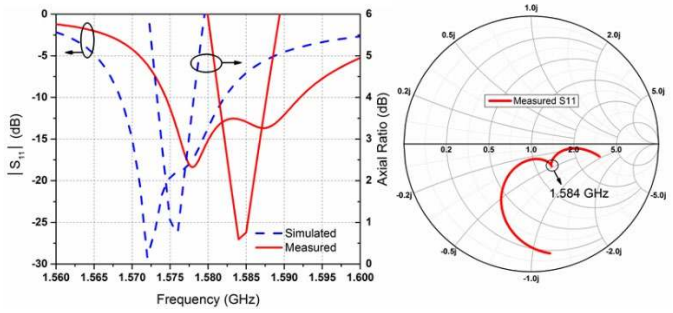

Fig. 9. Comparison of the measured and simulated results of the prototype HCP antenna as functions of the source frequency. (a) $|S_{11}|$ and AR values. (b) Measured S_{11} values on a Smith Chart.

As shown in Fig. 9(b), a dip is clearly observed in the Smith chart plotted $|S_{11}|$ values. It occurs at 1584 MHz where the best CP radiation happens (i.e., AR_{min} = 0.6 dB). Thus, the realization of the HCP antenna's two offset resonances arising from its electric and magnetic NFRP elements is verified experimentally, as are the associated operating principles.

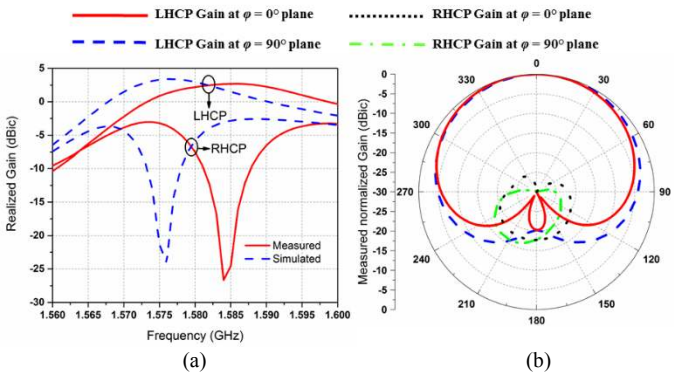

Fig. 10. Comparison of the measured and simulated results for the HCP antenna prototype. (a) LHCP and RHCP realized gain values as functions of the source frequency. (b) The measured normalized gain patterns at the measured operating frequency, 1.584 GHz.

The measured and simulated realized gain values are compared in Fig. 10(a) as functions of the source frequency. The measured normalized realized gain patterns at 1584 MHz are shown in Fig. 10(b). The measured LHCP peak realized gain value was 2.7 ± 0.3 dBic at 1.584 GHz, where ± 0.3 dB is the stated accuracy of the SATIMO StarLab system [43]. All the measurement tolerances given in this paper are in accordance with its performance datasheet. The 2.7 dBic is the normalization factor, which is 0.6 dB lower than the original simulated value, 3.3 dBic. Confirmed by additional simulations, this discrepancy arises from the presence of the long balun and coax cable. In the optimized design simulations that yielded the 3.3 dBic value, the coax is only 2.5 mm long and no balun is present. Again, in the experimental configuration, the balun is 46 mm long and the coax is 60 mm long. Simulating it, a 3.08 dBic maximum realized gain value was obtained, i.e., the presence of the long coax and balun introduced a reduction, 0.22 dB, of the maximum value. Thus, the actual difference between the measured and simulated values is only 0.308 dB, which is quite acceptable given the measurement system's stated accuracy of ± 0.3 dB. Note that the measured RHCP and LHCP behaviors are separated by more than 15 dB, again in reasonable agreement with the simulated results.

The measured (simulated) FTBR is 17.7 ± 2.5 dB (15.6 dB) at 1.584 GHz. Note that the simulated 15.6 dB FTBR value is obtained from the corresponding experimental setup model with the 60 mm long coaxial cable and the balun. The simulated FTBR value reaches 21.0 dB for the antenna model with only the 2.5 mm short coax and no balun, as presented in Sec III. B. Thus, the measured and simulated values agree reasonably well (again within the measurement system's accuracy [43]) and very good Huygens cardioid-shaped CP radiation patterns were demonstrated. The realized gain patterns in the two vertical planes ($\varphi = 0°$ and $\varphi = 90°$) are very similar in their main beam region (the upper half space). The measured half power gain beamwidth is more than 120° ± 5%. The measured antenna efficiency is shown in Fig. 11(a). The total antenna efficiency values, i.e., the ratio of the total radiated power to the total input power, at 1583, 1584, 1585 and 1586 MHz were 68%, 68%, 69% and 70%, respectively. These efficiency values are quite good for such a small-sized antenna with Huygens CP performance. The measured 3dB AR beamwidth is more than 180° centered on the broadside direction and, hence, it covers the entire +z half space as shown in Fig. 10(b). The measured radiation results further confirm the HCP ESA prototype operates as predicted.

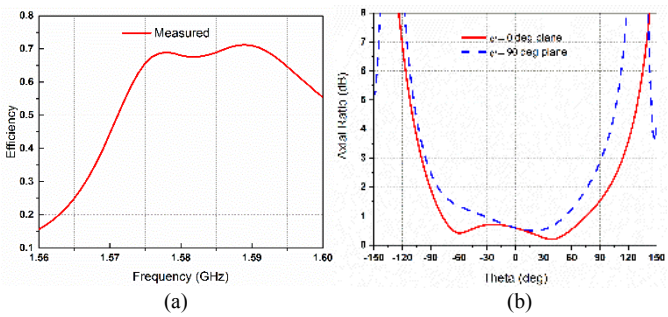

Fig. 11. Measured antenna parameters. (a) Total efficiency as functions of the source frequency. (b) AR beamwidth in the two vertical planes: $\varphi = 0°$ and $\varphi = 90°$ at 1.584 GHz.

VI. Conclusions

An electrically-small Huygens circularly-polarized antenna, its performance characteristics, and their verification with measured results were presented in this paper. The concept of integrating the NFRP EAD and CLL crossed elements to achieve the HCP behavior was explained. Parameter studies of the key variables were discussed to establish engineering design guidelines. A prototype of the optimized HCP ESA was fabricated and tested; the experimental results confirmed its operating principles and simulated performance characteristics. Due to its small size, high radiation efficiency, and CP Huygens patterns that have wide gain and AR beamwidths, this HCP ESA may be an excellent candidate for a variety of narrowband systems associated with GPS, WPT, and RFID applications.

VII. Acknowledgements

The authors would like to thank Prof. Y. Jay Guo, University of Technology Sydney, for his support of these efforts; Dr. Ming-Chun Tang from Chongqing University for his advices, Dr. Hang Wong from City University of Hong Kong, Mr. Shulin Chen from University of Technology Sydney and Dr. Thomas C. Baum from Royal Melbourne Institute of Technology (RMIT) University for their assistance in the measurement campaign.

References

[1] S. Lim, R. L. Rogers and H. Ling, "A tunable electrically small antenna for ground wave transmission," *IEEE Trans. Antennas Propag*., vol. 54, no. 2, pp. 417–421, Feb. 2006.

[2] J. Oh and K. Sarabandi, "Low profile vertically polarized omnidirectional wideband antenna with capacitively coupled parasitic elements," *IEEE Trans. Antennas Pro*pag., vol. 62, no. 2, pp. 977–982, Feb. 2014

[3] W. Hong, Y. Yamada, and N. Michishita, "Low profile small normal mode helical antenna achieving long communication distance," *in Proc. Int. Workshop Antenna Technol. (iWAT)* , Chiba, Japan, Mar. 2008, pp. 167–170.

[4] H. Wong, W. Lin, L. Huitema and E. Arnaud, "Polarization reconfigurable multi-dipole antenna for biomedical applications," *IEEE Trans. Biomed. Circuits Syst*., Jan. 2017, DOI: 10.1109/TBCAS.2016.2636872.

[5] J. Zhang and Y. Long, "A novel metal-mountable electrically small antenna for RFID tag applications with practical guidelines for the antenna design," *IEEE Trans. Antennas Propag*., vol. 62, no. 11, pp. 5820–5829, Nov. 2014.

[6] Y. Yamada, W. G. Hong, W. H. Jung, and N. Michishita, "High gain design of a very small normal mode helical antenna for RFID tags," i*n Proc. IEEE TENCON* , Taipei, Taiwan, Oct./Nov. 2007.

[7] P. Jin and R. W. Ziolkowski, "Multi-frequency, linear and circular polarized, metamaterial-inspired near-field resonant parasitic antennas," *IEEE Trans. Antennas Propag.*, vol. 59, pp. 1446-1459, May 2011

[8] N. Zhu, R. W. Ziolkowski, and H. Xin, "A metamaterial-inspired, electrically small rectenna for high-efficiency low power harvesting and scavenging at the GPS L1 frequency," *Appl. Phys. Lett*., vol. 99, 114101, Sep. 2011.

[9] I. J. Yoon and H. Ling, "Realizing efficient wireless power transfer using small folded cylindrical helix dipoles," *IEEE Antennas Wireless Propag. Lett.*, vol. 9, pp. 846–849, 2010.

[10] W. Lin and H. Wong, "Wideband circular polarization reconfigurable antenna with L-shaped feeding probes," *IEEE Antennas Wirel. Propag. Lett*., April, 2017, DOI: 10.1109/LAWP.2017.2699289.

[11] W. Lin and H. Wong, "Multi-polarization reconfigurable circular patch antenna with L-shaped probes," *IEEE Antennas Wirel. Propag. Lett*., Jan. 2017, DOI: 10.1109/LAWP.2017.2648862.

[12] C. A. Balanis, 3rd Ed., *Antenna Theory*. New York: John Wiley & Sons, 2005.

[13] J. L. Volakis and K. Sertel, "Narrowband and wideband metamaterial antennas based on degenerate band edge and magnetic photonic crystals," *Proc. IEEE*, vol. 99, no. 10, pp. 1732–1745, Oct. 2011.

[14] R. W. Ziolkowski, P. Jin, and C.-C. Lin, "Metamaterial-inspired engineering of antennas," *Proc. IEEE*, vol. 99, no. 10, pp. 1720–1731, Oct. 2011.

[15] Y. Dong and T. Itoh, "Metamaterial-based antennas," *Proc. IEEE*, vol. 100, no. 7, pp. 2271–2285, Jul. 2012.

[16] M. M. H. Armanious et al., "An electrically small conical folded dipole antenna for use as a compact, self-resonant mesoband high-power microwave source," *IEEE Trans. Antennas Propag*., vol. 62, no. 12, pp. 5960–5967, Dec. 2014.

[17] S. R. Best, "Electrically small resonant planar antennas: Optimizing the quality factor and bandwidth," *IEEE Antennas Propag. Mag*., vol. 57, no. 3, pp. 38–47, Jun. 2015.

[18] M. Hosseini, D. M. Klymyshyn, G. Wells, and X. Liu, "Short and open circuited EBG resonator antennas: Miniaturization with a shorting plate and dielectric loading," *IEEE Trans. Antennas Propag*., vol. 63, no. 10, pp. 4305–4314, Oct. 2015.

[19] R. F. Harrington, "On the gain and beamwidth of directional antennas," IEEE Trans. Antennas Propag., vol. 6, no. 3, pp. 219–225, Jul. 1958.

[20] R. F. Harrington, "Effect of antenna size on gain, bandwidth and efficiency," *J. Res. Nat. Bureau Standards*, vol. 64-D, pp. 1–12, Jan./Feb. 1960.

[21] M. Gustafsson, M. Cismasu, and B. L. G. Jonsson, "Physical bounds and optimal currents on antennas," *IEEE Trans. Antennas Propag.*, vol. 60, no. 6, pp. 2672-2681, Jun. 2012.

[22] O. S. Kim, "Electrically small circularly polarized spherical antenna with air core," in *Proc. 7th European Conference on Antennas and Propagation, EuCAP 2013*, Gothenburg, Sweden, pp. 233-236, April 2013.

[23] O. S. Kim, "Minimum Q Electrically Small Antennas," *IEEE Trans. Antennas Propag.*, vol. 60, no. 8, pp. 3551-3558, Aug. 2012.

[24] A. Alù and N. Engheta, "Enhanced directivity from subwavelength infrared/optical nano-antennas loaded with plasmonic materials or metamaterials," *IEEE Trans. Antennas Propag.*, vol. 55, no. 11, pp. 3027--3039, Nov. 2007.

[25] R. W. Ziolkowski, "Low profile, broadside radiating, electrically small Huygens source antennas," *IEEE Access*, vol. 3, pp. 2644-2651, Dec. 2015.

[26] M. C. Tang, H. Wang and R. W. Ziolkowski, "Design and testing of simple, electrically small, low-profile, Huygens source antennas with broadside radiation performance," *IEEE Trans. Antennas Propag.*, vol. 64, no. 11, pp. 4607–4617, Nov. 2016.

[27] M. C. Tang, B. Zhou, and R. W. Ziolkowski, "Low-profile, electrically small, Huygens source antenna with pattern-reconfigurability that covers the entire azimuthal plane," *IEEE Trans. Antennas Propag*., vol. 65, no. 3, pp. 1063-1072, Mar. 2017.

[28] K. M. Luk and H. Wong, "A new wideband unidirectional antenna element," *Int. J. Microw. Opt. Technol*., vol. 1, no. 1, pp. 35–44, Jun. 2006.

[29] Y. J. Li, J. H. Wang, and K.-M. Luk, "Millimeter-wave multi-beam aperture-coupled magneto-electric dipole array with planar substrate integrated beamforming network for 5G applications," *IEEE Trans. Antennas Propag.*, DOI: 10.1109/TAP.2017.2681429.

[30] K. M. Luk and B. Wu, "The magnetoelectric dipole: A wideband antenna for base stations in mobile communications," *Proc. IEEE*, vol. 100, no. 7, pp. 2297–2307, Jul. 2012.

[31] L. Ge and K.-M. Luk, "A low-profile magneto-electric dipole antenna," *IEEE Trans. Antennas Propag.*, vol. 60, no. 4, pp. 1684-1689, Apr. 2012.

[32] H.-J. Seo and A. A. Kishk, "Wideband magnetic-electric antenna with linear single or dual polarization," Prog. Electromagn. Res., vol. 155, pp. 53–61, Mar. 2016.

[33] H.-J. Seo and A. A. Kishk, "Wideband linear and dual-polarized antenna based on Huygens' source principle," in *Proc. 30th URSI General Assembly Sci. Symp*., Istanbul, Turkey, 2011, pp. 1–4.

[34] M. C. Tang, T. Shi, and R. W. Ziolkowski, "A study of 28 GHz, planar, multi-layered, electrically small, broadside radiating, Huygens source antennas," *IEEE Trans. Antennas Propag*., May. 2017, DOI: 10.1109/TAP.2017.2700888.

[35] K. Kang, Y, Shi and C. H. Liang, "A wideband circularly polarized magneto-electric dipole antenna," *IEEE Antennas Wireless Propag. Lett*., DOI: 10.1109/LAWP.2017.2660521, Jan. 2017.

[36] M. J. Li and K. M. Luk, "Wideband magnetoelectric dipole antennas with dual polarization and circular polarization," *IEEE Antennas Propag. Mag.*, vol. 57, no. 1, pp. 110–119, Feb. 2015.
[37] L. J. Chu, "Physical limitations of omni-directional antennas," *J. Appl. Phys.*, pp. 1163–1175, Dec. 1948.
[38] A. D. Yaghjian and S. R. Best, "Impedance, bandwidth, and Q of antennas," *IEEE Trans. Antennas Propag.*, pp. 1298–1324, Apr. 2005.
[39] M. Gustafsson, C. Sohl, and G. Kristensson, "Illustrations of new physical bounds on linearly polarized antennas," *IEEE Trans. Antennas Propag.*, vol. 57, no. 5, pp. 1319–1327, May 2009.
[40] C. Kilgus, "Resonant quadrafilar helix," *IEEE Trans. Antennas Propag.*, vol. AP-17, pp. 349–351, 1969.
[41] Q. X. Chu, W. Lin, W. X. Lin and Z. K. Pan, "Assembled dual-band broadband quadrifilar helix antennas with compact power divider networks for CNSS application," *IEEE Trans. Antennas Propag.*, vol. 61, no.2, pp.516–523, Feb. 2013.
[42] P. Jin and R. W. Ziolkowski, "Multi-frequency, linear and circular polarized, metamaterial-inspired near-field resonant parasitic antennas," *IEEE Trans. Antennas Propag.*, vol. 59, pp. 1446-1459, May 2011.
[43] *Data Sheet of StarLab near-field antenna measurement system* (2017). [Online]. http://www.mvg-world.com/en/system/files/starlab_2014.pdf.

Wei LIN received his PhD degree in Electronic Engineering from City University of Hong Kong, Hong Kong SAR in August 2016. He received the Master and Bachelor degrees, both in Electronic Engineering, at the South China University of Technology, Guangzhou, China in July 2012 and July 2009, respectively. He worked as a Research Associate at the Nanyang Technological University, Singapore from August 2012 to August 2013.

He is currently a postdoc research fellow with the Global Big Data Technologies Centre, University of Technology Sydney, Ultimo NSW, Australia. Dr. Lin was awarded the Outstanding Master Thesis Award from South China University of Technology in 2013. He received the Young Scientist Award at the IEEE Region 10 conference (TENCON) in December 2015 and a Talent Development Scholarship from the Hong Kong SAR Government in July 2016. Dr. Lin received the best poster paper award in the 2nd international conference on Electromagnetic Materials and Technologies for the Future (EM-MTF2017) in November 2017. His research interests include the designs of reconfigurable antennas, HF antennas, satellite antennas, millimeter wave antennas, terahertz devices, and their applications. He serves as reviewers for many IEEE and IET journals.

Richard W. Ziolkowski received the B.Sc. (magna cum laude) degree (Hons.) in physics from Brown University, Providence, RI, USA, in 1974; the M.S. and Ph.D. degrees in physics from the University of Illinois at Urbana-Champaign, Urbana, IL, USA, in 1975 and 1980, respectively; and the Honorary Doctorate degree from the Technical University of Denmark, Kongens Lyngby, Denmark in 2012.

He is currently a Distinguished Professor with the University of Technology Sydney, Global Big Data Technologies Centre, Ultimo NSW, Australia. He is also a Litton Industries John M. Leonis Distinguished Professor with the Department of Electrical and Computer Engineering and a Professor with the College of Optical Sciences at The University of Arizona. He was the Computational Electronics and Electromagnetics Thrust Area Leader with the Lawrence Livermore National Laboratory, Engineering Research Division, before joining The University of Arizona, Tucson, AZ, USA, in 1990. He was the Australian DSTO Fulbright Distinguished Chair in Advanced Science and Technology from 2014-2015. He was a 2014 Thomas-Reuters Highly Cited Researcher. His current research interests include the application of new mathematical and numerical methods to linear and nonlinear problems dealing with the interaction of electromagnetic and acoustic waves with complex linear and nonlinear media, as well as metamaterials, metamaterial-inspired structures, and applications-specific configurations.

Prof. Ziolkowski is a Fellow of the Optical Society of America (OSA, 2006), and of the American Physical Society (APS, 2016). He served as the President of the IEEE Antennas and Propagation Society in 2005. He is also actively involved with the URSI, OSA and SPIE professional societies.